

Cite this: *J. Mater. Chem. C*, 2025,
13, 4429

Extremely durable supercapacitor enabled by disordered porous carbon with a capacity retention up to 60 000 cycles†

Yu Ma, Chenmiao Ma, Jingya Wang, Xiaoqing Gao, Zepeng Li* and Yingdong Han *

Carbon-based materials, known for their green sustainability and high specific surface area, have long been favored as electrode materials with commercial prospects. However, they often fall short of delivering the expected performance in areas such as electrical conductivity and cycle stability. This paper reports a porous carbon material formed by combining NaCl crystals and citric acid. Relying on the hard template configuration, the molten pore-forming of NaCl crystals causes the citric acid base material to produce disordered porous carbon. Structural characterization and performance testing reveal that after high-temperature carbonization, the material generates numerous mesopores due to the evaporation etching of NaCl and has amorphous carbon with a highly disordered and dense structure. The resulting high specific surface area and abundant defects endow it with highly efficient electrochemical performance. Moreover, an enhanced specific capacitance of 81 F g⁻¹ at a current density of 0.5 A g⁻¹ and high capacitance retention rate of 98% after 60 000 cycles of the synthesized supercapacitor were obtained. This research offers a new avenue for the development of green energy and the design of electrode materials with commercial potential.

Received 8th November 2024,
Accepted 9th January 2025

DOI: 10.1039/d4tc04734f

rsc.li/materials-c

Introduction

Over the past few decades, supercapacitors have garnered significant attention as one of the most promising electrochemical energy storage devices. This is attributed to their appealing properties such as high power density, rapid charge–discharge rate, exceptional durability, safety, and reliability.^{1–4} For practical applications in the future, it is essential to manufacture high-performance supercapacitors that possess superior cycle life and high specific capacitance while maintaining a high energy density.⁵ Recently, porous carbon has emerged as one of the most efficient electrode materials for supercapacitors due to its excellent desired characteristics, including high chemical stability, high porosity, large specific surface area, and high electrical conductivity.^{6–8} Activated carbons have been intensively studied for supercapacitor electrode applications. These materials give rise to a category of supercapacitors known as electrical double layer capacitors (EDLCs), which are electrochemically stable and rely on physical adsorption processes.^{9,10} As a result, they can provide ultrahigh power density and excellent cycle life.

Compared with transition metal oxides, porous carbon materials generally exhibit lower specific capacitance, thereby limiting the overall performance of the supercapacitor.^{11,12} Among them, activated carbons hold a predominant share in commercial markets.¹³ However, commercial high-surface-area activated carbons typically possess moderate gravimetric capacitances in aqueous electrolytes. Generally, the enhancement of specific capacitance for supercapacitors can be achieved through the following modifications, such as engineering the surface functionality, pore structure, and compositing with other materials with pseudocapacitance (transition metal oxides/hydroxides or electrically conducting polymers).^{14–17} This has been intensively investigated and has been found to have positive effects on the electrochemical properties.

The hard template method is a commonly employed approach for preparing carbon electrode materials for supercapacitors. Injecting the precursor into the template for carbon material preparation enables the production of controllable porous carbon materials, offering an effective scheme for enhancing the arrangement of the material's pore structure.¹⁸ For instance, Rohan Bahadur *et al.*¹⁹ utilized KIT-6 silica as a hard template to synthesize ordered mesoporous carbides of fullerene and BCN. The high surface area and uniform pore size distribution provide a shortcut for ion charge transfer. After 6000 cycles at 5 A g⁻¹, the material exhibits ultra-capacitance

College of Science, Civil Aviation University of China, Tianjin, P. R. China.
E-mail: hansuo@126.com

† Electronic supplementary information (ESI) available. See DOI: <https://doi.org/10.1039/d4tc04734f>

stability close to 100%, and the capacitance is 171.2 F g^{-1} at 0.5 A g^{-1} . Zhang *et al.*²⁰ employed hollow carbon spheres (HCS) as a carbon structure template and polyaniline (PANI) as a precursor, in combination with cyclodextrin polymer (CDP). This promoted the further growth of polyaniline and further enhanced the charge and discharge performance of CDP-PANI/HCS. In a three-electrode system, the specific capacitance of PANI/HCS is 390 F g^{-1} at 1 A g^{-1} . After CDP polymerization, its specific capacitance can be increased to 569 F g^{-1} . CDP-PANI/HCS has an energy density of 24.5 W h kg^{-1} and a power density of 700 W kg^{-1} . Evidently, there is great potential for CDP-assisted improvement in the growth of PANI using HCS as a hard template. Wei *et al.*²¹ used flake $\text{Mg}(\text{OH})_2$ as a template and a reagent with oxygen-containing functional groups. All the above-mentioned methods have demonstrated the advantages and potential of hard templates in adjusting pores.

In this study, a simple, economical, and sustainable method of using NaCl as a hard template to prepare carbon electrode materials was employed. Here, citric acid monohydrate was used as a precursor, followed by a carbonization process to prepare a hierarchical porous carbon. By altering the content of the salt template in citric acid, the influence on the morphology and pores of carbon materials was analyzed, and its electrochemical performance was studied. Benefiting from the hierarchically porous structure, large specific surface area, and excellent conductivity, the $\text{HC}_2\text{-900}$ delivers superior supercapacitor performance with an improved specific capacitance (223 F g^{-1}) in aqueous KOH solution. Moreover, a symmetric supercapacitor was constructed, which exhibited significantly enhanced performance, *i.e.*, high specific capacity (81 F g^{-1} at 0.5 A g^{-1}), remarkable energy/power density (11.3 W h kg^{-1} at 499 W kg^{-1}), and excellent stability with a capacitance retention of $\sim 98.8\%$ after 60 000 cycles.

Results and discussion

The whole preparation process of sample $\text{HC}_2\text{-900}$ is illustrated in Fig. 1. Citric acid monohydrate is employed as the carbon source, while sodium chloride serves as the template agent. The active material is prepared *via* a simple freeze-drying and high-temperature annealing procedure. Subsequently, there is no extra necessity to treat sodium chloride with acid or alkali. During the final high-temperature process, most of the sodium chloride will be sublimated and eliminated. So porous carbon materials are formed after carbonization. After being washed multiple times with deionized water, a small amount of residual sodium chloride can be completely removed. Ultimately, a homogeneous porous carbon $\text{HC}_2\text{-900}$ will be obtained. The Fig. S1 (ESI[†]) presents the typical field emission scanning electron microscope (SEM) images of carbon material samples



Fig. 1 The schematic illustration of the fabrication of sample $\text{HC}_2\text{-900}$.

at different magnifications, demonstrating their intricate microstructures and confirming their highly dense amorphous mesoporous structures. Fig. S1a and b (ESI[†]) indicate that the directly carbonized C-900 without activation features a dense structure and a rough surface with no obvious porous structures. As the content of NaCl increases, Fig. S1c and d (ESI[†]) show that for the carbon material $\text{HC}_1\text{-900}$ activated by NaCl, the number of mesopores gradually rises and the pores gradually expand. Fig. S1e and f (ESI[†]) reveal that when the content of NaCl in sample $\text{HC}_2\text{-900}$ increases, more droplets are formed due to the melting of NaCl during high-temperature pyrolysis. The high mesopore content augments the specific surface area for ion attachment and enhances conductivity. However, Fig. S1g and h (ESI[†]) show that when the content of NaCl in $\text{HC}_3\text{-900}$ is excessively increased, the mesopore content becomes overly dense, leading to structural damage. The pores at the connections collapse, making the material more pulverized and resulting in a decreased specific surface area.

The TEM images of $\text{HC}_2\text{-900}$ are presented as follows. Fig. 2a and b display an obvious closed quasi-rectangular structure, which is a typical example of the NaCl salt template. Under high-temperature pyrolysis, NaCl particles with hard template configuration melt, leaving microporous vacancies. Fig. 2c shows that it has a highly dense shape structure and a highly wrinkled surface texture, indicating the existence of a large amount of amorphous carbon. The diffraction pattern in Fig. 2d shows an amorphous state, which is well consistent with the SEM results. In order to obtain insights into the formation mechanism of the porous skeleton in all samples, elemental mapping was carried out using an energy dispersive spectrometer (EDS), as depicted in Fig. S2 (ESI[†]). The C and O elements are distributed across the entire surface of the carbon skeleton. The elemental analysis results of all samples were also obtained as depicted in Fig. S3 (ESI[†]). It is evident that all samples comprise elements of C and O. Notably, the Au is originated from the testing preparation process. The content of C within all samples was determined to be approximately from 95.87 wt% to 88.77 wt%, respectively (Table S1, ESI[†]). Fig. S4

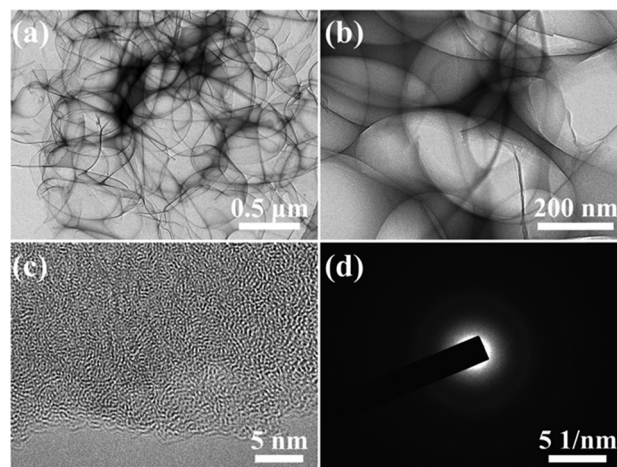


Fig. 2 (a)–(c) The typical TEM images and (d) SAED of sample $\text{HC}_2\text{-900}$.

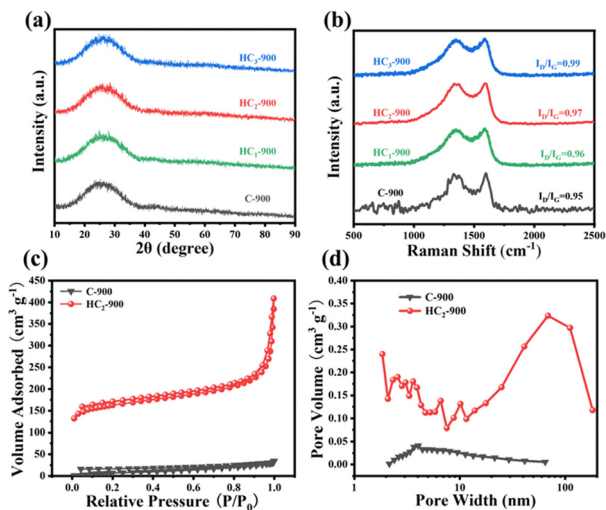


Fig. 3 (a) Typical XRD patterns and (b) representative Raman spectra of samples C-900, HC₁-900, HC₂-900 and HC₃-900. (c) N₂ adsorption-desorption isotherms, and (d) pore diameter distributions of samples C-900 and HC₂-900.

(ESI[†]) reports the Fourier-transform infrared spectroscopy (FTIR) spectrum of samples HC₂-900 and C-900 in the wavenumber range of 500–4000 cm⁻¹, showing the presence of various functional groups, which indicates the presence of oxygen containing functional groups such as carbonyl groups, hydroxyl groups and carboxyl groups. The band at 3435 cm⁻¹ represents the O–H stretching and vibrations of the absorbed water molecules. The band at 1601 cm⁻¹ is related to the stretching vibration of C=C and C=O. The bands at 2949, 2872 and 871 cm⁻¹ are associated with aliphatic (alkenes) and aromatic C–H, respectively. The appearance of a peak around 1072 cm⁻¹ indicates the existence of C–O bond in carboxylic acids, alcohols, phenols, and esters, respectively.²² On the one hand, the Fig. 3a presents the X-ray powder diffraction (XRD) spectrum of all samples. For the (002) crystal plane at 25 degrees, all the samples exhibit distinct broad peaks. Meanwhile, the diffraction peak intensity of the (100) crystal plane at 43 degrees is relatively low, suggesting that the graphitization degree of the samples is low and the degree of disorder is high.²³ This can lead to the generation of more defects and active sites.²⁴ The Raman spectrum of the sample further confirms that the D peak and G peak situated in the frequency bands of 1335 cm⁻¹ and 1595 cm⁻¹ are respectively attributed to sp³ hybridized defects and sp² hybridized graphite carbon.²⁵ The peak intensity ratio (I_D/I_G) is employed to represent the degree of graphitization.²⁶ As the amount of NaCl gradually increases, the I_D/I_G value rises from 0.95 to 0.99 (Fig. 3b), which is consistent with the results of element analysis, indicating that the number of defects gradually grows and there are more active sites. The improved surface wettability will facilitate the electrolyte penetrate into porous structure leading to the formation of a higher electrostatic double layer. The XRD and Raman spectra jointly confirm the successful preparation of salt-template carbon materials.

The pore structure and specific surface area of these samples were further analyzed by means of N₂ adsorption-desorption measurement diagrams. According to Fig. 3c, sample HC₂-900 presents a type IV adsorption curve, which implies a mesoporous structure.²⁷ At a relatively low pressure ($P/P_0 < 0.5$), the adsorption volume value of HC₂-900 is higher than that of C-900, which suggests the existence of abundant micropores in the base material.²⁸ The calculated surface area value of HC₂-900 (536 m² g⁻¹) is markedly higher than that of C-900 (28 m² g⁻¹). At P/P_0 of 0.9, the adsorption volume shows a sharp increase, indicating a large quantity of macropores. And from the pore size distribution diagram (Fig. 3d), it can be observed that the sample HC₂-900 shows a rich pore structure in the range of 1–10 nm. Moreover, the macropore volume in the range of 10–100 nm accounts for a larger proportion, conjointly reflecting a structure where micropores, mesopores, and macropores coexist, among which the latter two are preferable access for electrochemistry. Sample C-900 has a small amount of mesoporous structure, which may be caused by the escape of CO₂ and water decomposed from trace citric acid crystals at high temperature. The sample HC₂-900 has the largest average pore size (9.62 nm) with an average pore volume of 0.44 cm³ g⁻¹ than sample C-900 (6.63 nm and 0.03 cm³ g⁻¹, respectively), suggesting its highest surface-to-volume ratio, which could assist in maintaining a stable porous architecture for high rate capability. Therefore, the addition of NaCl can enhance the distribution of mesoporous structures under high-temperature pyrolysis conditions. The porous structure formed by evaporation and etching provides channels for the rapid transportation of ions.²⁹ Molecules are easily condensed by capillarity in mesopores to increase the adsorption amount, significantly improving its capacity for charge storage and promoting electrochemical effects. Thus, it can be seen that the reasonable adjustment of salts has a great influence on the specific surface area and pore volume of carbon materials. This material with a high specific surface area can provide a large electrode/electrolyte adsorption interface for energy storage devices.

Furthermore, the chemical compositions and atomic configurations in the HC₂-900 were investigated by an X-ray photoelectron spectroscopy (XPS) measurement. The XPS analysis of sample HC₂-900 indicates that it is primarily composed of C and O elements (as shown in the Fig. S5, ESI[†]). The fitting of C 1s (Fig. 4a) reveals that it mainly consists of C–C, C–O, and O–C=O. The fitting of O 1s (Fig. 4b) shows its functional

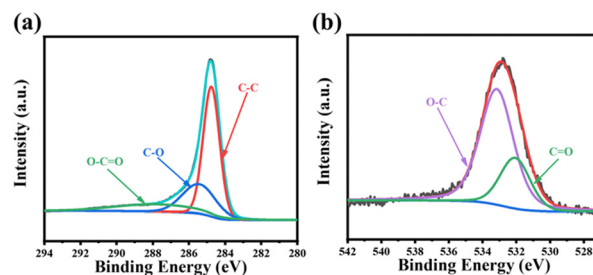


Fig. 4 High resolution XPS spectra of sample HC₂-900. (a) C 1s and (b) O 1s.

groups of O–C and C=O. It is believed that C=O can enhance the adsorption of ions by carbon materials and the wettability of electrodes and electrolytes, thereby promoting ion transfer.³⁰ Additionally, it can also form more edge defects, suggesting that the NaCl template can adjust the functional groups on the material surface and thus accelerate charge transport. The higher capacitance due to the presence of appropriate carbon content provides good electrical conductivity during the electrochemical reaction. All characterization experiments indicate that when NaCl is employed as salt template, it exerts a significant influence on the unique structure and high specific surface area of the electrode. This material can generate abundant active sites and defects. It has a short diffusion distance, high adsorption capacity, and diverse ion channels. As an effective electrode material for supercapacitors, it holds extremely great prospects.

The electrochemical behaviors of HC₂-900 when used as an electrode were analyzed in a three-electrode system with an aqueous KOH solution (6.0 M) as the electrolyte. For comparison, C-900, HC₁-900 and HC₃-900 were also tested under the same conditions. Fig. 5a shows the typical CV curves of all electrodes. At a scanning rate of 100 mV s⁻¹, all curves exhibit stable charge and discharge behavior. When the working potential is 1.1 V, all curves show a similar rectangular shape, indicating that the electrode has ideal capacitive behavior. It can be seen that the rectangular enclosed area of the HC₂-900 electrode is larger than that of the other electrodes, proving that the material has a higher specific capacitance due to its relatively larger specific surface area and abundant mesoporous content.

The GCD curves of the electrodes at 1 A g⁻¹ are shown in Fig. 5b. It is clearly seen that the charge–discharge time of the sample HC₂-900 is the longest, which is consistent with the

conclusion shown by the above CV curve. The charge and discharge curves of all samples show excellent symmetry and linear relationship, proving their typical electric double layer structure, ideal capacitive behavior and excellent electrical conductivity. At a current density of 1 A g⁻¹, the specific capacitance (223 F g⁻¹) of HC₂-900 is much higher than those of C-900 (46 F g⁻¹), HC₁-900 (119 F g⁻¹), and HC₃-900 (181 F g⁻¹). This is mainly due to the fact that its porous structure with large specific surface area and high adsorption can accelerate the transmission and diffusion rate of electrolyte ions at the electrode interface. The abundant mesopores of HC₂-900 are conducive to ion deposition and promote charge transfer reactions, which are important influencing factors for the application of supercapacitors.^{31,32} Even at a high current density of 20 A g⁻¹, a specific capacitance of 161 F g⁻¹ can be reached (Fig. 5c), with a capacitance retention rate of 72%, implying excellent electrochemical performance. In comparison, C-900, HC₁-900, and HC₃-900 electrodes exhibit a lower capacity of 3 F g⁻¹, 93 F g⁻¹ and 137 F g⁻¹ at the same current density (Fig. 5c). As shown in Fig. 5d, the EIS analysis of four samples during the charge storage process were further carried out. In the high-frequency region, HC₂-900 electrode has a lower charge transfer resistance, with a value of equivalent series resistance (R_s) 0.58 Ω . In addition, HC₂-900 also shows lower charge transfer resistance (R_{CT}) (0.13 Ω) than C-900 (0.6 Ω), HC₁-900 (0.14 Ω) and HC₃-900 (0.16 Ω). This proves that the reasonable adjustment of NaCl content can enable citric acid-derived carbon materials to have a better electron conduction rate and improve the obstruction of ion transfer. In the low-frequency region, the straight line of HC₂-900 tends to be vertical and has a greater slope, indicating lower transmission resistance. This is attributed to its large number of mesoporous structures leading to good charge transfer ability. These electrochemical characteristics of the HC₂-900 electrode material are more suitable for high-performance supercapacitors.

Furthermore, compared to the three-electrode system, the two-electrode system can evaluate the practical application of the supercapacitor more specifically. As shown in Fig. 6a, under different potential windows at the scan rate of 100 mV s⁻¹, the CV curve of HC₂-900 shows an obvious nearly rectangular shape without mutation. It has good stability and good capacitance. The GCD curves are plotted within different potential windows (Fig. 6b). In the range of 0–2 V, all curves show a linear relationship and good symmetry, demonstrating excellent capacitive reversibility. Even under different current densities from 0.5 to 40 A g⁻¹ (Fig. 6c), it still shows excellent reversibility and stability. At a current density of 0.5 A g⁻¹, an outstanding high specific capacitance of 82 F g⁻¹ is obtained. Even when the current density is 40 A g⁻¹, the capacitance of 17 F g⁻¹ is still maintained. EIS analysis was performed to understand the ion diffusion process (Fig. 6d), which proves that the internal resistance of the device is relatively low. The Bode plot (Fig. 6e) shows a shorter time constant (1211 ms), indicating that its charge and discharge stability is achieved faster and significantly improved electron transport and capacitive behavior. At the same time, the assembled supercapacitor shows excellent cycle stability with 98.8% capacitance retention after

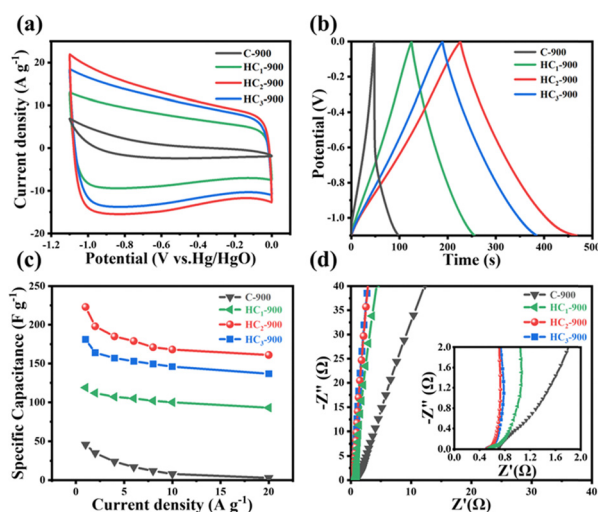


Fig. 5 Electrochemical performance of the samples in a three-electrode system. (a) CV curves at a scan rate of 100 mV s⁻¹. (b) GCD curves at the current density of 1 A g⁻¹. (c) Specific capacitances at different current densities, (d) Nyquist plots of samples C-900, HC₁-900, HC₂-900 and HC₃-900.

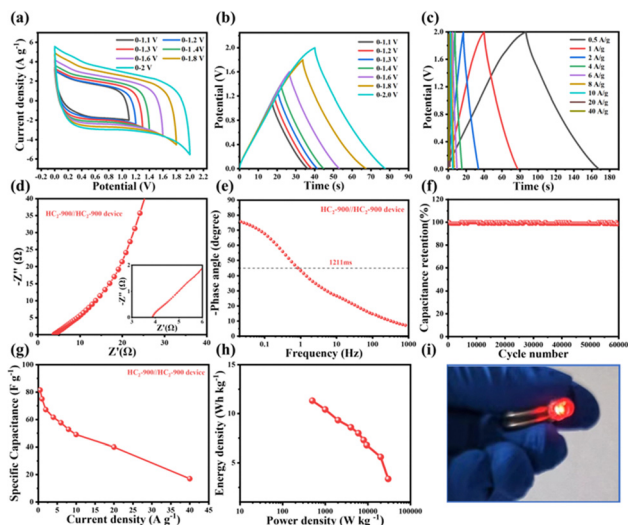


Fig. 6 Electrochemical performance of HC₂-900 electrode in symmetrical two-electrode system: (a) CV curves at various voltage ranges (100 mV s⁻¹). (b) GCD curves at various voltage ranges (1 A g⁻¹). (c) GCD curves at current densities from 0.5 to 40 A g⁻¹. (d) The Nyquist plot. (e) Impedance phase angle vs. frequency. (f) Cycling stability at a density of 4 A g⁻¹ upon 60 000 cycles. (g) Specific capacitances at different current densities. (h) Ragone plots. (i) A photo of two tandem devices powering a red LED.

60 000 cycles at a current density of 4 A g⁻¹ (Fig. 6f), which is superior to carbon-based supercapacitors reported in other literatures (Table S2, ESI[†]). The specific capacitance of the device is calculated at different current densities (Fig. 6g). The energy and power densities are calculated as shown in Fig. 6h. At the power density of 499 W kg⁻¹, the symmetric supercapacitor delivered an encouraging energy density of 11.3 W h kg⁻¹, indicating that HC₂-900 has good energy storage characteristics. Two assembled button cells can successfully light up a red light-emitting diode (LED), which operates at the voltage of 3 V (Fig. 6i). This is mainly attributed to the abundant mesoporous structure in the material, which is conducive to high-quality ion transmission.

Conclusions

In conclusion, this paper reports a simple and green method for fabricating electrode materials. By combining NaCl crystals and citric acid, an efficient porous carbon energy storage material is formed. NaCl crystals are used for pore formation, and melting during the carbonization process increases the specific surface area of the material. This change makes its surface highly dense. The amorphous structure increases its contact area with the electrolyte. The obtained sample has a rich mesoporous structure, providing channels for rapid ion transport and greatly improving its charge storage. The material generates abundant active sites and defects, endowing it with excellent electrochemical performance. The HC₂-900 electrode exhibits a high capacitance of 225 F g⁻¹ in 6 M KOH aqueous electrolyte. Moreover, the assembled supercapacitor also shows excellent rate capability and good energy density.

The energy density is 11.3 W h kg⁻¹ with the power density of 499 W kg⁻¹ in a 1 M Na₂SO₄ aqueous electrolyte. After more than 60 000 cycles, it has an excellent stability with a capacitance retention rate of more than 98%. This research provides a more fundamental reference for the synthesis of carbon material electrodes based on sustainable green development and offers another solution for products with commercial prospects.

Data availability

The data that support the findings of this study are available from the corresponding author upon reasonable request.

Conflicts of interest

There are no conflicts to declare.

Acknowledgements

This work was supported by the Scientific Research Project of Tianjin Municipal Education Commission (No. 2022KJ060).

Notes and references

- 1 A. Nayak, B. Bhushan, S. Kotnala, N. Kukretee, P. Chaudhary, A. R. Tripathy, K. Ghai and S. Laxmi Mudliar, *Mater. Today*, 2023, **73**, 227–232.
- 2 H. A. Khan, M. Tawalbeh, B. Aljawrneh, W. Abuwatfa, A. Al-Othman, H. Sadeghifar and A. G. Olabi, *Energy*, 2024, **295**, 131043.
- 3 B. Chen, D. Wu, T. Wang, Q. Liu and D. Jia, *Chem. Eng. J.*, 2024, **486**, 150353.
- 4 B. Chen, D. Wu, T. Wang, F. Yuan and D. Jia, *Chem. Eng. J.*, 2023, **462**, 142163.
- 5 W. Bo, H. Zhang, G. Yin, L. Zhang and J. Qin, *Carbon Resour. Convers.*, 2023, **9**, 91.
- 6 Y. Feng, J. Jiang, Y. Xu, S. Wang, W. An, Q. Chai, U. H. Prova, C. Wang and G. Huang, *Carbon*, 2023, **211**, 118105.
- 7 X. Chen, J. Ma, X. Sun, C. Zhao, J. Li and H. Li, *Int. J. Biol. Macromol.*, 2024, **258**, 128759.
- 8 F. H. Gourji, T. Rajaramanan, A. Kishore, M. Heggertveit and D. Velauthapillai, *ACS Omega*, 2023, **8**, 23446–23456.
- 9 J. Liu, L. Ma, Y. Zhao, H. Pan, H. Tang and H. Zhang, *Chem. Eng. J.*, 2021, **411**, 128573.
- 10 J. Zhang, W. Liu, M. Du, Q. Xu, M. Hung, R. Xiang, M. Liao, X. Wang, B. Wang, A. Yu and K. Zhang, *Carbon Energy*, 2024, e625.
- 11 M. Czagany, S. Hompoth, A. K. Keshri, N. Pandit, I. Galambos, Z. Gacsi and P. Baumli, *Mater.*, 2024, **17**, 702.
- 12 J. Liang, Y. Zhang, X. Tang, H. Song, L. Qin and X. Fan, *Mater. Today Commun.*, 2024, **38**, 108371.
- 13 Y. Yang, H. Du, A. Wang, C. Lu, D. Sun, C. Lu, X. Wang, Z. Xiao and X. Ma, *J. Colloid Interf. Sci.*, 2024, **673**, 657–668.
- 14 P. An, W. Li, Y. Leng, T. Zhang, J. Zhu, T. Li, W. Li and Y. Han, *Polymer*, 2024, **300**, 127004.

- 15 J. Huang, C. Liu, Y. Jin and J. Chen, *Chem. Eng. J.*, 2023, **461**, 141930.
- 16 B. Xue, J. Xu and R. Xiao, *Chem. Eng. J.*, 2023, **454**, 140192.
- 17 B. Li, L. Zhang, Z. Zhao, Y. Zou, B. Chen, X. Fu, F. Wang, S. Long, W. Guo, J. Liang and M. Ye, *Chem. Eng. J.*, 2024, **487**, 150730.
- 18 J. Yin, W. Zhang, N. A. Alhebshi, N. Salah and H. N. Alshareef, *Small Methods*, 2020, **4**, 1900853.
- 19 R. Bahadur, G. Singh, Z. Li, B. Singh, R. Srivastava, Y. Sakamoto, S. Chang, R. Murugavel and A. Vinu, *Carbon*, 2024, **216**, 118568.
- 20 W. Zhang, J. Guo, T. Chen, S. Park, M. Bae, Y. Cho, G. Diao, L. Lin and Y. Piao, *Mater. Today Chem.*, 2023, **33**, 101733.
- 21 W. Wei, W. Liu, Z. Chen, R. Xiao, Y. Zhang, C. Du, L. Wan, M. Xie, J. Chen and Z. Tian, *Appl. Surf. Sci.*, 2020, **509**, 144921.
- 22 T. Nguyen, B. Yoon, T. Nguyen, E. Oh, Y. Ma, M. Wang and J. Suhr, *Carbon*, 2023, **206**, 383–391.
- 23 Y. Zeng, W. Zhao, X. Li, X. Chen, J. Song, X. Wu and Z. Huang, *Mater. Today Commun.*, 2023, **36**, 106623.
- 24 X. Liu, D. Lyu, C. Merlet, M. J. A. Leesmith, X. Hua, Z. Xu, C. P. Grey and A. C. Forse, *Science*, 2024, **384**, 321–325.
- 25 Y. Ma, Y. Ge, D. Gao, Z. Li, M. Du, X. Xing, R. Feng and Y. Han, *J. Mater. Chem. C*, 2023, **11**, 10502–10508.
- 26 S. K. Das, L. Pradhan, B. K. Jena and S. Basu, *Carbon*, 2023, **201**, 49–59.
- 27 Y. Ma, D. Chen, Z. Fang, Y. Zheng, W. Li, S. Xu, X. Lu, G. Shao, Q. Liu and W. Yang, *Proc. Natl. Acad. Sci. U. S. A.*, 2021, **118**, 21.
- 28 J. Ouyang, M. Zhang, W. Xiong, L. Zhou, L. Zhao, Z. Li, C. Zhou, H. Chen, Y. Luo, S. Fang and R. H. Baughman, *J. Colloid Interface Sci.*, 2024, **671**, 145–153.
- 29 Y. Li, C. Kong, Z. Du, J. Zhang, X. Qin, J. Zhang, C. Li, Y. Jin and S. Wang, *Energy Adv.*, 2024, **3**, 904–915.
- 30 M. Jalalah, H. Han, A. K. Nayak and F. A. Harraz, *Adv. Compos. Hybrid Mater.*, 2024, **7**, 20.
- 31 M. Zhou, P. Wang, Y. Yu, W. Ma, Z. Cai, F. Ko, M. Li and Q. Wang, *Energy*, 2023, **278**, 127705.
- 32 Y. Ren, Y. Liu, S. Wang, Q. Wang, S. Li, W. Wang and X. Dong, *Carbon Energy*, 2022, **4**, 527–538.